Article

Aligned grains and scattered light found in gaps of planet-forming disk

https://doi.org/10.1038/s41586-023-06648-7

Received: 7 June 2023

Accepted: 14 September 2023

Published online: 15 November 2023

Check for updates

Ian W. Stephens[1]✉, Zhe-Yu Daniel Lin[2], Manuel Fernández-López[3], Zhi-Yun Li[2], Leslie W. Looney[4], Haifeng Yang[5], Rachel Harrison[4,6], Akimasa Kataoka[7], Carlos Carrasco-Gonzalez[8], Satoshi Okuzumi[9] & Ryo Tazaki[10,11]

Polarized (sub)millimetre emission from dust grains in circumstellar disks was initially thought to be because of grains aligned with the magnetic field[1,2]. However, higher-resolution multi-wavelength observations[3–5] and improved models[6–10] found that this polarization is dominated by self-scattering at shorter wavelengths (for example, 870 μm) and by grains aligned with something other than magnetic fields at longer wavelengths (for example, 3 mm). Nevertheless, the polarization signal is expected to depend on the underlying substructure[11–13], and observations until now have been unable to resolve polarization in multiple rings and gaps. HL Tau, a protoplanetary disk located 147.3 ± 0.5 pc away[14], is the brightest class I or class II disk at millimetre–submillimetre wavelengths. Here we show deep, high-resolution polarization observations of HL Tau at 870 μm, resolving polarization in both the rings and the gaps. We find that the gaps have polarization angles with a notable azimuthal component and a higher polarization fraction than the rings. Our models show that the disk polarization is due to both scattering and emission from the aligned effectively prolate grains. The intrinsic polarization of aligned dust grains is probably more than 10%, which is much higher than that expected in low-resolution observations (about 1%). Asymmetries and dust features that are not seen in non-polarimetric observations are seen in the polarization observations.

We used the Atacama Large Millimeter/submillimeter Array (ALMA) in Full Stokes mode at 0.033″ (4.9 au) resolution to observe both the total emission and polarized emission from HL Tau (Methods). The linear polarization data (Stokes *Q* and *U*) were combined with data from previous observations[4] for increased sensitivity, which resulted in a slightly coarser resolution of about 0.0345″ (5.1 au). Figure 1 shows the polarization morphology of HL Tau overlaid on the Stokes *I* image. Vectors are plotted in a grid with a separation of 0.0198″ (that is, sampled slightly less than Nyquist sampling), for a total of 2,067 displayed vectors. The number of independent vectors detected towards HL Tau is an order of magnitude more than that detected previously[4], and about an order of magnitude more than the previously best-resolved disk in polarization[15].

Given the long integration times, the Stokes *I* image of HL Tau is at much higher fidelity than what has been done before[16], and it is presented in Fig. 2. Previously HL Tau had seven identified dark bands[16] or gaps, but our observations show an eighth gap towards the edge of the disk, which we measure to be at a radius of approximately 0.73″ or 107.5 au. We rename the gaps from their old nomenclature[16] (D1–D7) to a nomenclature that shows their distance in au, as the distance of 147.3 pc has now been accurately determined by Gaia[14].

The previous observations of HL Tau[4] showed polarization vectors close to uniform polarization and parallel to the minor axis of the disk with polarization fractions around 1%. Figure 1 shows a non-uniform polarization morphology and higher polarization fractions. The orientations of the polarization vectors in the rings are mostly uniform, whereas the vectors in the gaps have a strong azimuthal component, showing two distinct brackets around the disk centre. Figure 3 shows the polarization fraction and polarized intensities along with the eight gaps overlaid on HL Tau. Along with what is seen in Fig. 1, there are three key features of the polarization:

1. Polarization fractions are typically much higher in the gaps (reaching up to 3.7%) than in the rings. Even the polarized intensity is frequently higher in the gaps.
2. Polarization vectors are usually uniformly aligned along the minor axis, but there is a notable azimuthal component in the gaps. Notably, the first gap (D14) has a ring of polarized intensity with azimuthally oriented polarization directions that surrounds the inner disk.
3. The polarized fractions and intensities are larger along the major axis than the minor axis.

The first feature is further quantified in Fig. 4, which shows cuts in Stokes *I*, polarization fraction and polarized intensity along the major

[1]Department of Earth, Environment and Physics, Worcester State University, Worcester, MA, USA. [2]Department of Astronomy, University of Virginia, Charlottesville, VA, USA. [3]Instituto Argentino de Radioastronomía, CCT-La Plata (CONICET), Villa Elisa, Argentina. [4]Department of Astronomy, University of Illinois, Urbana, IL, USA. [5]Kavli Institute for Astronomy and Astrophysics, Peking University, Beijing, People's Republic of China. [6]School of Physics and Astronomy, Monash University, Clayton, Victoria, Australia. [7]National Astronomical Observatory of Japan, Tokyo, Japan. [8]Instituto de Radioastronomía y Astrofísica (IRyA), Universidad Nacional Autónoma de México (UNAM), Morelia, Mexico. [9]Department of Earth and Planetary Sciences, Tokyo Institute of Technology, Tokyo, Japan. [10]Université Grenoble Alpes, CNRS, Institut de Planétologie et d'Astrophysique (IPAG), Grenoble, France. [11]Astronomical Institute, Tohoku University, Sendai, Japan. ✉e-mail: istephens@worcester.edu

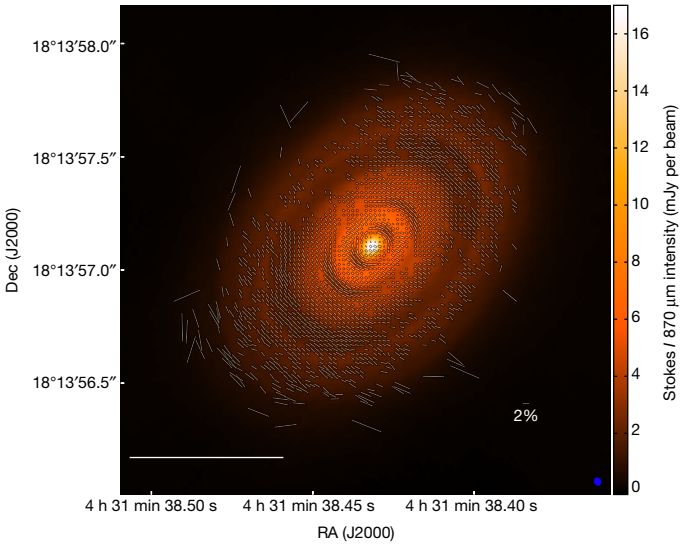

Fig. 1 | The 870-μm polarization morphology overlaid on the total-intensity images of HL Tau. The length of the vectors is proportional to the percentage of light that is polarized (*P*), with a 2% scale bar shown at the bottom right. A 100 AU scale bar is shown on the bottom left. The vectors are plotted when both their total intensity (Stokes *I*) and the polarized intensity are detected at a 3σ level, and for $P < 10\%$. Vectors with $P < 0.5\%$ are drawn as thinner lines. The resolution (beam) is shown as a small blue ellipse at the bottom right. Dec, declination; RA, right ascension.

axis. For the inner three gaps, there are local peaks in both polarized intensity and fraction. By contrast, for Stokes *I* rings, there are local troughs, except the very central Stokes *I* peak.

The fact that the polarized intensity is stronger in the gaps was unexpected, as there is less dust. Furthermore, the Stokes *I* is typically more symmetric along the major axis than the polarized intensity. For example, the Stokes *I* fluxes along the cut for the first gap (D14) differ by 6%, whereas the polarized intensity and fraction differ by about 30%. An increased asymmetry of these quantities is not expected along the major axis of an axisymmetric disk for polarization because of scattering or grain alignment, suggesting there are features in the disk not seen in Stokes *I*. For example, there could be a slight warp in the disk, a difference along the major axis in the dust scale height or a difference in dust grain properties (for example, composition, albedo or sizes)[6].

By contrast, for an inclined dust disk that is not geometrically thin, asymmetries are fully expected along the minor axis, with the near side of the disk (that is, the part of the disk closer to the observer) expected to be more polarized than the far side of the disk[17]. The near side of HL Tau is towards the bottom right[16], yet the ring between the first two gaps has a more polarized intensity towards the far side of the disk. This again suggests that there are some asymmetries along the minor axis. However, interior to the first gap (that is, the central bright emission), the polarized intensity is higher on the near side compared with that on the far side, as expected for a thicker dust disk.

Building on previous work[9], we create a model that can broadly explain the three key features mentioned earlier, with the details of the model in the Methods. Our attempts at a model with polarization solely from the scattering of spherical grains, which is also applicable to randomly aligned grains, could mostly reproduce the three key features. However, it cannot re-create the large polarized intensity with an azimuthally oriented polarization morphology[13] in the first gap (D14). By including both polarized thermal emission and scattering of aligned effectively prolate grains spinning about its long axis, the model not only explains all three features but also fits them more closely than the scattering-only model. In our model, we find that the long axis of a grain is aligned azimuthally around the disk, which is also consistent with the polarization morphology at 3.1 mm (ref. 18). The effective sizes of the prolate grains follow an $a^{-3.5}$ power-law distribution[19] with a maximum grain size of 100 μm and creates the general scattering polarization morphology. Prolate-like grains are favoured over oblate-like grains because oblate grains have difficulty producing the observed polarized morphology and intensity along the minor axis observed in D14. Nevertheless, there is probably a mix of grain shapes, and our model suggests that the observations are most consistent with the effective shapes that are predominantly prolate.

This model explains why the polarization is higher in the gaps than in the rings (key feature 1) because the rings have higher optical depth that minimizes polarization from grain alignment because of a higher dichroic extinction. In turn, this also allows for an azimuthal component only in the gaps (key feature 2) because the optical depth of the rings is too high to produce significant polarized emission from grain alignment, but still sufficiently low enough in the gaps that the azimuthal pattern from aligned grains dominates the uniform pattern from scattering. The model also produces larger polarization fractions

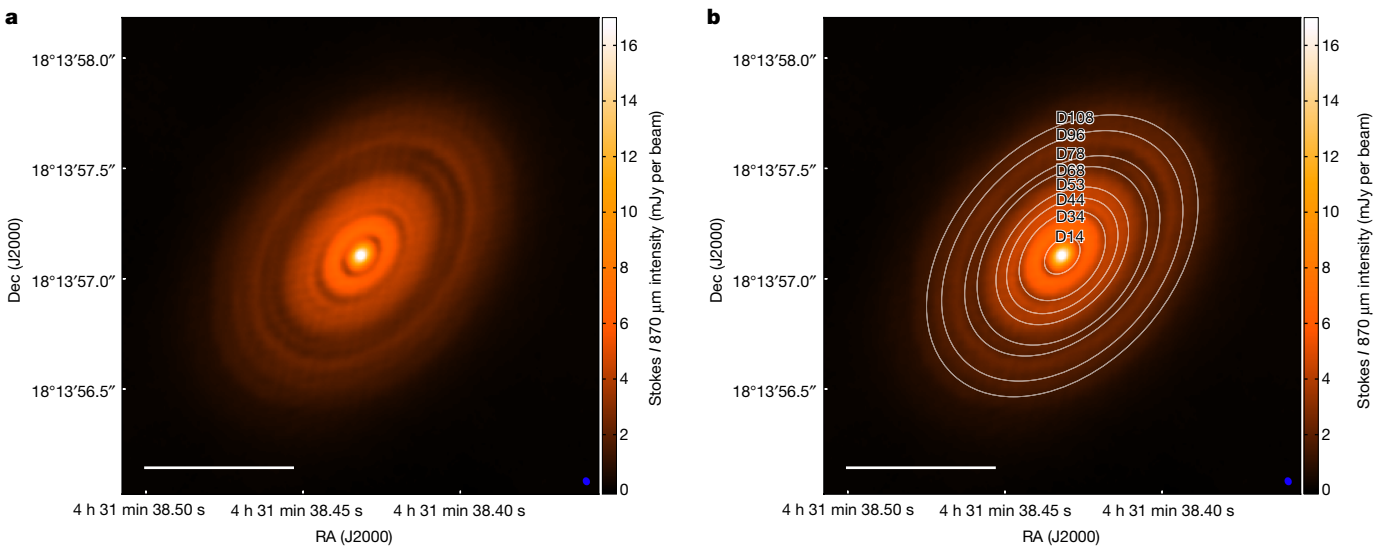

Fig. 2 | The 870-μm total-intensity (Stokes *I*) image of HL Tau. a,**b**, The resolution (beam) is shown as a small blue ellipse at the bottom right. **a** and **b** are identical, except that **b** has ellipses at the locations of the gaps[16], which includes the previously unidentified eighth gap. The number on the label of each gap indicates the semimajor axis length in AU. Scale bars, 100 AU. Dec, declination; RA, right ascension.

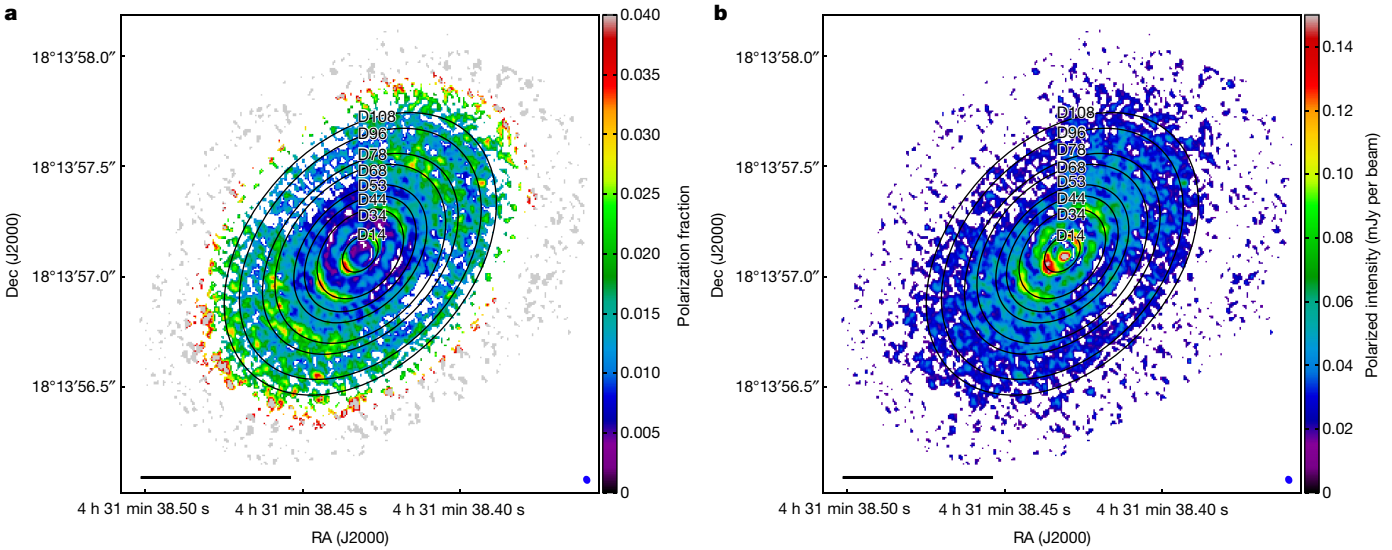

Fig. 3 | Polarization fraction and intensity maps of HL Tau. a,**b**, The gaps in the disk that were presented in Fig. 2 are shown. The resolution (beam) is shown as a small blue ellipse at the bottom right. Scale bars, 100 AU.

and intensities along the major axis than the minor axis (key feature 3) because the polarization from grain alignment and inclination-induced scattering[7] are constructive along the major axis and destructive along the minor axis.

To match the polarization fraction of the model to that of the observations, we can adjust the intrinsic polarization of dust grain emission by changing the elongation of the grain. Assuming the grains are perfectly aligned, we find that an intrinsic polarization between 10% and 15% (prolate grain short- to long-axis aspect ratio of around 0.85) is needed to match the observations. Although the observations show typical polarization levels of 2–3% in the gaps, the model suggests they are being smoothed (beam averaged) by the low polarization levels of the rings. As such, higher resolution observations are likely to have much higher polarization fractions. The high intrinsic polarization is similar to that found in the interstellar medium[20,21], although the grains in the disk have grown to a much larger size. The intrinsic aspect ratio is probably even smaller than 0.85 because that value assumed 100% alignment efficiency.

Furthermore, the model shows that rings are optically thick and must be a factor of approximately 10 times stronger in the gaps, which has been suggested in multi-wavelength studies of HL Tau[22]. We can come to this conclusion just with the polarization observations at a single wavelength. As the rings are much more optically thick, most of the mass must be in these optically thick rings. These rings are thus the probable reservoirs for the future formation of planetesimals.

Grains of about 100 μm size are probably not a unique solution and would underestimate the intensity of the image at longer wavelengths (for example, 3 mm). Models could be further fine-tuned, but they

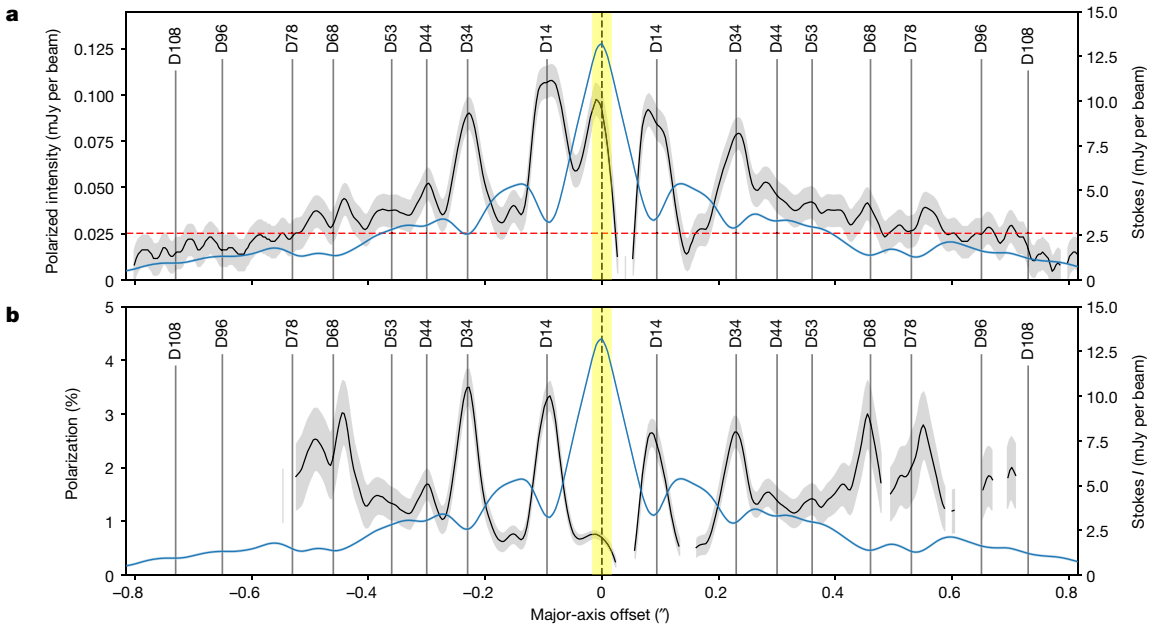

Fig. 4 | Stokes *I*, polarized intensity, and polarization fraction profiles along the major axis of HL Tau (southeast to northwest). a,**b**, The Stokes *I* cut is in blue, and the polarized intensity (**a**) and fraction (**b**) are in black. The shaded grey area shows the standard deviation (1σ). The shaded yellow region shows the resolution of the observations along the major axis (0.032″). The red line in **a** is the 3σ cutoff for polarized intensity. Panel **b** shows only polarization fractions measured above the 3σ level; therefore, the black curve does not extend to the outer edge of the disk. Gaps are labelled with vertical lines.

are degenerate because of different parameters, including grain size, composition, albedo, porosity, alignment efficiency and shape[10,23,24]. Multi-wavelength high-resolution observations are necessary to overcome these degeneracies and accurately constrain grain sizes. Nevertheless, these models show that both grain scattering and alignment are at play, with scattering dominating the polarization in the rings and aligned grains in the gaps. Finally, it is worth mentioning that even these models cannot explain polarization asymmetries across the major and minor axes, indicating that polarization may show dust properties across a planet-forming disk that cannot be seen by non-polarimetric continuum observations.

Online content

Any methods, additional references, Nature Portfolio reporting summaries, source data, extended data, supplementary information, acknowledgements, peer review information; details of author contributions and competing interests; and statements of data and code availability are available at https://doi.org/10.1038/s41586-023-06648-7.

1. Rao, R., Girart, J. M., Lai, S.-P. & Marrone, D. P. Detection of a magnetized disk around a very young protostar. *Astrophys. J. Lett.* **780**, L6 (2014).
2. Stephens, I. W. et al. Spatially resolved magnetic field structure in the disk of a T Tauri star. *Nature* **514**, 597–599 (2014).
3. Kataoka, A. et al. The evidence of radio polarization induced by the radiative grain alignment and self-scattering of dust grains in a protoplanetary disk. *Astrophys. J. Lett.* **844**, L5 (2017).
4. Stephens, I. W. et al. ALMA reveals transition of polarization pattern with wavelength in HL Tau's disk. *Astrophys. J.* **851**, 55 (2017).
5. Harrison, R. E. et al. Dust polarization in four protoplanetary disks at 3 mm: further evidence of multiple origins. *Astrophys. J. Lett.* **877**, L2 (2019).
6. Kataoka, A. et al. Millimeter-wave polarization of protoplanetary disks due to dust scattering. *Astrophys. J.* **809**, 78 (2015).
7. Yang, H., Li, Z.-Y., Looney, L. & Stephens, I. Inclination-induced polarization of scattered millimetre radiation from protoplanetary discs: the case of HL Tau. *Mon. Not. R. Astron. Soc.* **456**, 2794–2805 (2016).
8. Yang, H. Size limit of superparamagnetic inclusions in dust grains and difficulty of magnetic grain alignment in protoplanetary disks. *Astrophys. J.* **911**, 125 (2021).
9. Lin, Z.-Y. D. et al. Thermal emission and scattering by aligned grains: plane-parallel model and application to multiwavelength polarization of the HL Tau disc. *Mon. Not. R. Astron. Soc.* **512**, 3922–3947 (2022).
10. Lin, Z.-Y. D. et al. (Sub)millimetre dust polarization of protoplanetary discs from scattering by large millimetre-sized irregular grains. *Mon. Not. R. Astron. Soc.* **520**, 1210–1223 (2023).
11. Pohl, A. et al. Investigating dust trapping in transition disks with millimeter-wave polarization. *Astron. Astrophys.* **593**, A12 (2016).
12. Ohashi, S. & Kataoka, A. Radial variations in grain sizes and dust scale heights in the protoplanetary disk around HD 163296 revealed by ALMA polarization observations. *Astrophys. J.* **886**, 103 (2019).
13. Lin, Z.-Y. D. et al. Validating scattering-induced (sub)millimetre disc polarization through the spectral index, wavelength-dependent polarization pattern, and polarization spectrum: the case of HD 163296. *Mon. Not. R. Astron. Soc.* **496**, 169–181 (2020).
14. Galli, P. A. B. et al. The Gould's Belt Distances Survey (GOBELINS). IV. Distance, depth, and kinematics of the Taurus star-forming region. *Astrophys. J.* **859**, 33 (2018).
15. Ohashi, S. et al. Two different grain size distributions within the protoplanetary disk around HD 142527 revealed by ALMA polarization observation. *Astrophys. J.* **864**, 81 (2018).
16. ALMA Partnership. et al.The 2014 ALMA Long Baseline Campaign: observations of the strongly lensed submillimeter galaxy HATLAS J090311.6+003906 at z=3.042. *Astrophys. J. Lett.* **808**, L4 (2015).
17. Yang, H., Li, Z.-Y., Looney, L. W., Girart, J. M. & Stephens, I. W. Scattering-produced (sub) millimetre polarization in inclined discs: optical depth effects, near-far side asymmetry and dust settling. *Mon. Not. R. Astron. Soc.* **472**, 373–388 (2017).
18. Yang, H., Li, Z.-Y., Stephens, I. W., Kataoka, A. & Looney, L. Does HL Tau disc polarization in ALMA band 3 come from radiatively aligned grains? *Mon. Not. R. Astron. Soc.* **483**, 2371–2381 (2019).
19. Mathis, J. S., Rumpl, W. & Nordsieck, K. H. The size distribution of interstellar grains. *Astrophys. J.* **217**, 425–433 (1977).
20. Planck Collaboration. *Planck* intermediate results. XIX. An overview of the polarized thermal emission from Galactic dust. *Astron. Astrophys.* **576**, A104 (2015).
21. Planck Collaboration. *Planck* intermediate results. XX. Comparison of polarized thermal emission from Galactic dust with simulations of MHD turbulence. *Astron. Astrophys.* **576**, A105 (2015).
22. Pinte, C. et al. Dust and gas in the disk of HL Tauri: surface density, dust settling, and dust-to-gas ratio. *Astrophys. J.* **816**, 25 (2016).
23. Tazaki, R., Tanaka, H., Kataoka, A., Okuzumi, S. & Muto, T. Unveiling dust aggregate structure in protoplanetary disks by millimeter-wave scattering polarization. *Astrophys. J.* **885**, 52 (2019).
24. Yang, H. & Li, Z.-Y. The effects of dust optical properties on the scattering-induced disk polarization by millimeter-sized grains. *Astrophys. J.* **889**, 15 (2020).

Methods

Observations and data reduction

The observations presented in this paper are from the ALMA project 2019.1.01051.S, which were combined in part with the ALMA project 2016.1.00115.S, as discussed below (principal investigator: I. Stephens). The project 2019.1.01051.S observed HL Tau in Full Stokes polarization at 870 μm using two different array configurations, C-5 and C-8, which together provide baselines from 54 kλ to 13,300 kλ. The observations were taken from June to October 2021, with a total time on source of 18.7 h. Each of the tracks observed used between 39 and 43 antennas. We tuned the correlator for four 1.75-GHz spectral windows centred at sky frequencies of 336.5 GHz, 338.5 GHz, 348.5 GHz and 350.5 GHz. We downloaded the raw measurement sets of the observations and applied the initial calibration delivered in a pipeline by the ALMA staff.

The Stokes *I* continuum emission was created using only the 2019.1.01051.S data. They were self-calibrated using three iterative phase-only calibration and cleaning stages, with progressively lower time intervals down to 10.4 s. We then removed nine channels contaminated by line emission from $C^{17}O$, SO_2 and CH_3CO in different spectral windows, which account for around 3% of the total bandwidth. Following the analysis by the Disk Substructures at High Angular Resolution Project (DSHARP) team[25], before combining the datasets of the two different configurations, we aligned the disk peak in both datasets using CASA programs fixplanets and phaseshift and re-scaled their fluxes using gencal. The final Stokes *I* image has a root mean square (rms) noise level of 15.9 μJy per beam, which gives a signal-to-noise ratio of 1,073 at the peak. It was constructed using a robust weighting of 0.5, and the synthesized beam was 35.5 milliarc seconds (mas) × 30.5 mas at a position angle of 22° (measured anticlockwise from north). We also attempted to combine these Stokes *I* data with the HL Tau Science Verification data[16], but we found that these data reduced the signal to noise.

For producing the polarization images, we combined data from the ALMA project 2016.1.00115.S (ref. 4), but self-calibrating in the same manner as above, and aligning the peak position and re-scaling the flux of the visibilities to match that of the 2019.1.01051.S combined data. This project consisted of shorter baselines from the ALMA C-4 configuration, which gave baselines as short as 15.5 kλ. The frequency setup was the same as the 2019.1.01051.S data, and we also removed the same nine channels with line contamination. The Stokes *I* image of this track had notable side lobes, and added only additional noise to the 2019.1.01051.S Stokes *I* data (rms noise level of 15.9 μJy per beam without C-4 versus 39.7 μJy per beam with C-4). As such, for Figs. 1 and 2, we did not include the C-4 data for Stokes *I*, but we did for the polarization vectors. However, for the rest of the figures in the paper and those in the extended data, we included the C-4 in Stokes *I*, because a consistent beam and spatial sampling is needed for proper calculations (that is, polarization fraction) and comparisons of radial cuts. After a Högbom CLEAN deconvolution interactive process in CASA using a robust parameter of 0.5, the final beam size for the polarization data was 37.4 mas × 31.8 mas with a position angle of 26°, reaching an rms noise level of 8.4 μJy per beam. We found that combining these data (2016.1.00115.S and 2019.1.01051.S) added just more than 500 vectors to Fig. 1, with these vectors primarily corresponding to locations with low-level Stokes *I* emission. As polarization fraction and intensity can be only positive, there exists a bias towards the positive values. As such, we de-bias all polarization data as given in previous works[26,27]. As mentioned in the plots, the vectors are all detected at a 3σ level and have $P < 10\%$. The vectors that have $P > 10\%$ are few and are towards the outer disk, and thus are potentially interferometric artefacts or random noise above the 3σ level. Including these in Fig. 1 makes the other vectors less clear, as these vectors are long given the 2% scale bar.

The ALMA also measures Stokes *V*, which we also imaged. Without considering instrumental effects, the Stokes *V* from the 2021 observational data is positive and seems to be detected significantly in some areas of the disk with a circular polarization fraction of a few tenths of a per cent. However, the 2017 band 7 polarization data[4] are inconsistent with these observations because they suggest that the Stokes *V* is negative and has similarly low circular polarization fractions. As the ALMA is not currently commissioned to measure significant (3σ) polarization at levels less than 1.8% because of instrumental effects (primarily beam squint), we consider any observational indication of circular polarization as probably from instrumental artefacts.

Linear polarization modelling

The goal of this model is to demonstrate the main features of the observed Stokes *I*, linear polarized intensity and linear polarization fraction through radiation transfer modelling of scattering of aligned prolate grains using a recently developed approach[9]. The model presented here is essentially identical to that presented in ref. 9, except we consider rings and gaps within the disk rather than just a smooth density profile. Incorporating this substructure when matching the model to observations enables new constraints on the dust parameters. In the following, we briefly describe the model and its setup, but we refer to ref. 9 for more details.

Scattering-induced dust polarization depends on grain properties such as size, shape and composition[6,10,23,24], all of which are uncertain. Polarization data for a single wavelength do not allow a precise determination of these properties in general; our case is no exception. We adopt the oft-used dust properties from the DSHARP[28]. Specifically, we adopt a complex refractive index of $m \approx 2.30 + 0.0228i$ at $\lambda = 870$ μm and a power-law grain-size distribution[19] of $a^{-3.5}$. From here, we fix the minimum grain size $a_{\rm min}$ to 0.1 μm and the maximum grain size $a_{\rm max}$ to 100 μm, and we assume the grains have no porosity. As the scattering in the Rayleigh regime under consideration is dominated by grains containing most of the volume (and thus the mass), the value of $a_{\rm min}$ has little effect on the model for the chosen size distribution. The value of $a_{\rm max}$ is set by the requirement that (compact spherical) grains of the order of 100 μm in size are needed to dominate the scattering of 870 μm (band 7) photons efficiently[6]. It is well-known that this size is in tension with the larger (mm and cm) grain sizes commonly inferred from the dust opacity index[3,10,24], but it is beyond the scope of this paper to address the tension in detail.

The inclusion of scattering greatly complicates the radiative transfer equation[29]. Although Monte Carlo techniques are effective in handling scattering in the 3D structure of disks, completely dealing with aligned grainsis challenging, and much of the research in this area has been limited to spherical or randomly aligned grains[30–36]. The radiative transfer simplifies markedly if each local patch of the dust disk is approximated by a plane-parallel slab[9]. The plane-parallel approximation is reasonable because the dust layer responsible for the (sub)millimetre continuum emission of HL Tau is geometrically very thin vertically, with a dust scale height of approximately 1 AU and a radius of 100 AU, based on the lack of an azimuthal variation of the gap width[22].

The dust opacities and the scattering properties depend on the composition, shape and size of the grains. The grain shape is uncertain and expected to be at least somewhat irregular. To facilitate quantitative modelling, we represent the grains with effective spheroids[37], scattering properties of which can be calculated using the T-matrix method[38,39]. To be explicit, when we refer to prolate grains, we refer to grains that are effectively prolate (including intrinsically elongated grains and grains spinning around their longest axis) and likewise oblate grains for effectively oblate grains (including intrinsically oblate grains and grains spinning around their shortest axis)[18]. As there is already evidence that polarized thermal emission from effective prolate grains can explain the azimuthal polarization pattern in the HL Tau disk at band 3 (3.1 mm) better than that from effective oblate grains[9,18,40], we choose to use prolate grains to model the similar azimuthal pattern observed in the gaps in our high-resolution band 7 data as well. As shown in Extended Data Fig. 1a, they naturally produce the parallel-to-the-major-axis

polarization orientations observed in the first gap at the locations along the minor axis. This feature is difficult, if not impossible, to produce with effectively oblate grains, which will be shown later in this section. The polarization fraction of the thermal radiation emitted by aligned prolate grains depends on the alignment efficiency and intrinsic degree of elongation of the grain, which are uncertain. In particular, the former can depend on the grain size, especially if the grains are aligned by a mechanism depending on internal alignment, which is size-dependent[41]. In our model, these effects are encapsulated in a dimensionless free parameter, s, which is the effective aspect ratio of the adopted prolate grain. For simplicity, we assume the same value of s for grains of all sizes in the power-law size distribution, with the expectation that the value inferred from model comparison with observations is indicative of the effective aspect ratio of mainly those grains contributing most to the thermal emission—the largest grains for the adopted size distribution.

To obtain the dust continuum intensity from the plane-parallel slab, we need the alignment direction of prolate grains, temperature T and surface density Σ at each line of sight. For simplicity, we assume the disk is axisymmetric, and we prescribe T and Σ as a function of the cylindrical radius R. As indicated above, we consider only toroidally aligned, prolate grains that do not depend on the radius. To limit the parameter space, we use a power-law prescription for the temperature profile

$$T = T_{10}(R/10)^{-0.5}, \tag{1}$$

where T_{10} is the temperature at a radius of 10 au. We fix the power-law index to −0.5 because it is the expectation of a passively irradiated disk[42,43] and is consistent with previous constraints[44].

As an approximation to the set of multiple rings, we construct the dust surface-density distribution as a summation of individual axisymmetric Gaussian rings. The surface density of the ith ring is defined by its absorption optical depth through

$$\tau_i(R) = \tau_{c,i}\exp\left(-\frac{1}{2}\left(\frac{R-C_i}{W_i}\right)^2\right), \tag{2}$$

where C_i is the location of the centre of the ring, W_i is the scale width and $\tau_{c,i}$ is the optical depth at the ring centre. The surface density is related to the optical depth through $\sum_i(R) = \tau_{c,i}/\kappa_{ext}$ where κ_{ext} is the dust extinction opacity. As the grains are non-spherical, the extinction opacity should depend on the viewing direction of the grain, but here we take κ_{ext} as the extinction opacity averaged over all solid angles.

Similarly, the inner disk (denoted by a subscript a) is prescribed as a power-law with an exponential taper also defined through the optical depth by

$$\tau_a(R) = \tau_{c,0}\left(\frac{R}{R_0}\right)^{-p}\exp\left(\frac{R}{R_0}\right)^{1.5} \tag{3}$$

where $\tau_{c,0}$ is the characteristic optical depth and R_0 is the characteristic radius. The surface density of the complete disk is simply a summation of the rings and the inner disk and is expressed as

$$\Sigma(R) = \Sigma_a(R) + \sum_{i=1}^{N}\Sigma_i(R) \tag{4}$$

where N is the total number of rings.

Following the methodology in ref. 9, creating the complete image of the disk involves piecing together each patch of the disk for which the intensity is approximated by the emergent intensity of the plane-parallel slab. First, we produce the image of the disk in the principal frame, in which the image coordinates, x_p and y_p, are along the disk minor and major axes direction given some inclination i (i = 0 means face-on). The Stokes convention of ALMA is based on the International Astronomical Union (1974) convention[45]. For clarity, let Q_p and U_p be the Stokes parameters Q and U in the principal frame with the International Astronomical Union (1974) convention. The disk inclination produces polarization parallel to the disk minor axis (along the x_p direction), which means a positive Stokes Q_p. Second, because the observations are defined in right ascension and declination (that is, sky frame), we convert the Stokes parameters Q and U in the principal frame (that is, Q_p and U_p) to those in the sky frame (denoted by subscript s, as Q_s and U_s) using

$$Q_s = Q_p\cos2\eta - U_p\sin2\eta \tag{5}$$

$$U_s = Q_p\sin2\eta + U_p\cos2\eta, \tag{6}$$

where η is the position angle (anticlockwise from north) of the disk minor axis on the far side. Stokes I in the principal frame and that in the sky frame (Stokes I_s) are equal in value. From previous observations[16], we adopt an inclination of i = 46.7° and a position angle of the disk major axis of 138.02°. Given that the blue-shifted outflow is to the northeast[16], the position angle of the far side of the disk is at η = 48.02°. Last, when comparing the model to the observations of finite resolution, we convolve the model with the elliptical Gaussian beam of the observation.

We try to match the Stokes I_s and the linear polarization fraction along the major and minor axes of the disk. The Stokes I_s profile constrains the locations and widths of the rings, the temperature T_{10} and, in part, the optical depth. The polarization fraction constrains a_{max}, s and the optical depth[17]. Extended Data Table 1 shows the adopted parameters. In general, each bright band identified from the observations can be reproduced using a single Gaussian ring. We find that a_{max} = 100 μm matches well with the observations, and such a fit is similar to previous results based on polarization[40,46]. As a reference, the adopted a_{max} gives κ_{ext} ~3.12 cm^2 g^{-1}, which provides the conversion from the optical depth to the dust surface density. Although we find that the adopted parameters are adequate to broadly reproduce the observations, we warn that the parameters may not be unique in producing such features[10,23,24].

Extended Data Fig. 1a shows the resulting model for the Stokes I and polarization vectors that can be compared with Fig. 1. Extended Data Fig. 1b,c shows the polarization fraction and polarized intensity that can be compared with Fig. 3. The close similarity between the model and the observed image demonstrates that scattering by aligned prolate grains together with their polarized thermal emission and extinction can readily capture the main observed features, as discussed in the main text. First, the polarization fractions and polarized intensities (Extended Data Fig. 1b,c) are mostly larger along the major axis. The origin is because the thermal polarization and inclination-induced polarization are constructive along the major axis, but destructive along the minor axis[9]. Moreover, beam averaging of the rings and gaps also contributes to this azimuthal variation. The polarization from the rings that are uniformly parallel to the minor axis of the disk is constructive with the thermal polarization from the gaps along the major axis, but destructive along the minor axis.

Second, along the major axis, the polarization fraction is much higher in the gaps than in the rings, which we can easily identify for the innermost five gaps (D14, D34, D44, D68 and D78) as shown in Extended Data Fig. 1b. This is also the case for polarized intensity although easily seen at only D34 and D44 in Extended Data Fig. 1c. To show the trend more clearly, we show the one-dimensional profile along the major axis in Extended Data Fig. 2, and compare the model with the observation. We also do this for the minor axis in Extended Data Fig. 3. To show the direction of the polarization fraction, we also plot $q_p \equiv Q_p/I_p$ in Extended Data Fig. 3. As the polarization along the principal axes is either parallel or perpendicular to the minor axis direction for the disk model, using q_p alone is sufficient and its absolute value corresponds to p. A positive q_p means polarization parallel to the disk minor axis, whereas a negative q_p means polarization parallel to the disk major axis. For the

observation, we calculate its Q_p using equation (5) given the observed Q_s and U_s. The model can capture the distribution of the Stokes *I* and its anti-correlation with the polarization fraction.

Qualitatively, the anti-correlation is a natural result of the varying optical depth of the rings and gaps. Thermal polarization is most prominent when the emitting material is optically thin. However, when the optical depth increases, dichroic extinction from the same material causes the thermal polarization to drop[9,17,47]. By contrast, scattering, and thus polarization from scattering, becomes effective only when the optical depth reaches the order of unity or larger[17]. Therefore, the optically thick rings can have large Stokes *I* but low *p*, whereas the optically thinner gaps can have low Stokes *I* and large *p*.

For quantitative comparisons, we also show the cuts of the model image before convolution. The units of Stokes *IQU* are scaled by the same factor as the convolved model for easier comparison. Convolution averages the intensities of the rings and gaps, but the polarization from the gaps is more affected than the polarization from the rings. Before convolution, the polarization fraction in the gaps is much higher than the polarization fraction after convolution. For example, at the first gap (D14), the polarization is about 7% before convolution, but appears as about 4.5% after convolution.

Furthermore, the thermal polarization from toroidally aligned prolate grains can explain the polarization in the minor axis of the first gap (D14), which is perpendicular to the disk minor axis (opposite to the inclination-induced polarization). In Extended Data Fig. 3, we show the cut along the minor axis. As defined above, the positive offset is along the far side of the disk. The convolved model can capture similar levels of the polarization fraction in the inner disk, the first gap (D14) and the ring between D14 and D34 (the first ring). Effects of beam averaging are more prominent along the minor axis because the gap is narrower in projection. Before convolution, the polarization fraction in D14 is about 5%, but seems to be about 1.7%. However, at the inner disk, the peak polarized intensity and the peak polarization fraction are not at the centre as predicted from the model, but shifted to the near side (southwest; Fig. 3). The shift can at least, in part, be explained by the near-far-side asymmetry of a geometrically thick inner dust disk[17]. The model cannot capture the near-far-side asymmetry because the image is built from plane-parallel slabs that are more applicable for geometrically thin disks.

We find that the aspect ratio of the prolate grain is $s = 0.85$ if perfectly aligned. Larger values of *s* make the polarization in the gap too strong, whereas smaller values of *s* make the elliptical polarization pattern disappear, particularly along the minor axis. For convenience, consider p_0 as the intrinsic level of polarization of the grain viewed edge-on (with the axis of symmetry perpendicular to the line of sight) in the optically thin limit (see ref. 9 for details). The prolate grain with $s = 0.85$ gives $p_0 \sim 12\%$, which is comparable to the observed levels of polarization in the envelope scale[48–51] and in the interstellar medium[20,21]. The high p_0 is necessary because it works against the optical depth of the gap itself and contamination from rings because of beam averaging.

By contrast, the outer regions along the minor axis do not show similar polarization perpendicular to the disk minor axis. As demonstrated in Extended Data Fig. 2, this can be explained by beam averaging of several rings with large enough optical depth. Going to even higher angular resolution and better sensitivity should mitigate the beam-averaging effects and uncover the thermal polarization from aligned grains, if any. This observation would make measurements of the radial distribution of grain alignment possible and provide constraints on the alignment mechanism.

The aspect ratio of $s = 0.85$ is much smaller than the $s \sim 0.97$ inferred from the lower angular resolution image of band 3 (3.1 mm) of HL Tau[9]. The latter is constrained by the approximately 2% polarization[3,4] along the outer regions of the minor axis of the disk in band 3 when assuming a smooth disk. The contrast suggests that polarization from aligned grains is diluted by polarization from the optically thick substructures even at band 3. Another possibility is by varying the levels of grain alignment efficiency or aspect ratios. The inner region may be more aligned and/or elongated, whereas the outer regions are less aligned and/or elongated. Going to longer wavelengths with similar angular resolution to resolve the rings and gaps will help distinguish the two scenarios. The lower optical depth at longer wavelengths increases the polarization fraction from aligned grains in the gaps, and also the decreased optical depth of the rings effectively increases the angular extent of the optically thin gaps making it easier to resolve the gaps.

If the dilution of large p_0 grains from optically thick substructure is true, then it has far-reaching implications for detecting grain alignment in disks in general. The ALMA has routinely detected polarization for disks although with only a few beams across the disk minor axis. Many sources show an elliptically oriented polarization pattern of a few per cent in the outer regions[5,52,53–55], which is similar to the previous low-angular resolution observations of HL Tau at band 3 (ref. 4). As most of these sources also have substructure, we speculate that the intrinsic polarization should be much higher just like the case of HL Tau and grain alignment may be frequent. More high-angular resolution studies of various sources that can resolve the gaps will be necessary to verify the frequency of aligned grains and their prevalence as a general phenomenon in disks.

We also rerun this identical analysis, but we use oblate grains with an aspect ratio of $s = 1.2$ and their short axes aligned radially in the disk. We do not consider oblate grains that are toroidally aligned, because the polarization would be radial and completely different from what is observed. The results are shown in Extended Data Fig. 4. In Extended Data Fig. 4a,b (bottom), we saturate the colour scale for the polarization fraction and morphology so that one can directly compare with Extended Data Fig. 1 for the prolate grain model. This model is inconsistent with the observations because the polarization direction is opposite to that observed in D14 along the minor axis. This discrepancy in polarization orientation can be removed in principle by increasing the aspect ratio of the oblate grain, but it would make the already excessively high polarization at locations along the major axis even higher. Decreasing the aspect ratio would render scattering more dominant, worsening the polarization orientation discrepancy in D14 along the minor axis and causing the polarization orientations in the gaps less azimuthal than observed.

To a certain extent, pure scattering of spherical or randomly aligned grains with the radiation anisotropy owing to the existence of rings and gaps can also produce the anti-correlation between Stokes *I* and *p* along the major axis. That is, the radiation anisotropy is greater in the gaps than in the rings, which leads to larger *p* (refs. 12,13,56). However, solely relying on radiation anisotropy will make it difficult to reproduce both the polarization direction and the high level of polarized intensity along the minor axis for the first gap (D14). Although each scattered photon can be highly polarized, the gaps need enough material to scatter enough photons from the rings to produce the high polarized intensity, but the polarization tends to follow the disk minor axis (inclination-induced polarization) with increasing optical depth.

Radiation anisotropy is not included given the plane-parallel nature of the model, and it is unclear how it will affect the inferred *s* (also degenerate with the alignment efficiency). As mentioned above, given the large optical depth seen along the midplane between each neighbouring patch of the disk, we can expect marginal contributions from radiation anisotropy that makes the use of the plane-parallel slab calculations favourable. This is probably the case for gaps too because the optical depth to the observer in the gaps is already greater than 1 (Extended Data Figs. 2 and 3). However, future refinements of the model will need to consider radiation anisotropy in 3D geometry. The strongest constraint for *s* comes from the polarization in the first gap (D14), in which the radiation anisotropy should be larger compared with the rings. The 3D geometry is also necessary to explain the near- and far-side asymmetry of the inner disk. Monte Carlo radiation transfer

codes that can easily handle radiation anisotropy in 3D geometry do not typically include scattering of aligned grains[31]. The superior quality of the data highlights the necessity for the development of 3D radiation transfer codes to include thermal emission and scattering of aligned grains in a self-consistent manner.

Data availability

This paper makes use of the following ALMA data: ADS/JAO.ALMA#2016.1.00115.S and ADS/JAO.ALMA#2019.1.01051. The observational data products generated and analysed during the current study are available in the Harvard Dataverse repository (https://dataverse.harvard.edu/dataverse/HLTau_Band7_Pol) under DOIs https://doi.org/10.7910/DVN/MM4V5M and https://doi.org/10.7910/DVN/7CQRBC. Raw ALMA data are available at ALMA Science (https://almascience.nrao.edu/aq/). Additional datasets (for example, modelling) are available from the corresponding author on request.

Code availability

This research made use of APLpy, an open-source plotting package for Python[57].

25. Andrews, S. M. et al. The Disk Substructures at High Angular Resolution Project (DSHARP). I. Motivation, sample, calibration, and overview. *Astrophys. J. Lett.* **869**, L41 (2018).
26. Hull, C. L. H. et al. TADPOL: a 1.3 mm survey of dust polarization in star-forming cores and regions. *Astrophys. J. Suppl. Ser.* **213**, 13 (2014).
27. Hull, C. L. H. & Plambeck, R. L. The 1.3 mm full-Stokes polarization system at CARMA. *J. Astron. Instrum.* **4**, 1550005 (2015).
28. Birnstiel, T. et al. The Disk Substructures at High Angular Resolution Project (DSHARP). V. Interpreting ALMA maps of protoplanetary disks in terms of a dust model. *Astrophys. J. Lett.* **869**, L45 (2018).
29. Yang, H. et al. Disc polarization from both emission and scattering of magnetically aligned grains: the case of NGC 1333 IRAS 4A1. *Mon. Not. R. Astron. Soc.* **460**, 4109–4121 (2016).
30. Whitney, B. A. & Wolff, M. J. Scattering and absorption by aligned grains in circumstellar environments. *Astrophys. J.* **574**, 205–231 (2002).
31. Dullemond, C. P. et al. RADMC-3D: a multi-purpose radiative transfer tool (Astrophysics Source Code Library, 2012).
32. Steinacker, J., Baes, M. & Gordon, K. D. Three-dimensional dust radiative transfer. *Ann. Rev. Astron. Astrophys.* **51**, 63–104 (2013).
33. Whitney, B. A. et al. Three-dimensional radiation transfer in young stellar objects. *Astrophys. J. Suppl. Ser.* **207**, 30 (2013).
34. Baes, M., Peest, C., Camps, P. & Siebenmorgen, R. Optical depth in polarised Monte Carlo radiative transfer. *Astron. Astrophys.* **630**, A61 (2019).
35. Reissl, S., Wolf, S. & Brauer, R. Radiative transfer with POLARIS. I. Analysis of magnetic fields through synthetic dust continuum polarization measurements. *Astron. Astrophys.* **593**, A87 (2016).
36. Peest, C., Camps, P., Stalevski, M., Baes, M. & Siebenmorgen, R. Polarization in Monte Carlo radiative transfer and dust scattering polarization signatures of spiral galaxies. *Astron. Astrophys.* **601**, A92 (2017).
37. Bohren, C. F. & Huffman, D. R. *Absorption and Scattering of Light by Small Particles* (Wiley, 1983).
38. Mishchenko, M. I., Travis, L. D. & Macke, A. Scattering of light by polydisperse, randomly oriented, finite circular cylinders. *Appl. Opt.* **35**, 4927–4940 (1996).
39. Mishchenko, M. I., Travis, L. D. & Mackowski, D. W. *T*-matrix computations of light scattering by nonspherical particles: a review. *J. Quant. Spectrosc. Radiat. Transf.* **55**, 535–575 (1996).
40. Mori, T. & Kataoka, A. Modeling of the ALMA HL Tau polarization by mixture of grain alignment and self-scattering. *Astrophys. J.* **908**, 153 (2021).
41. Hoang, T. & Lazarian, A. Grain alignment induced by radiative torques: effects of internal relaxation of energy and complex radiation field. *Astrophys. J.* **697**, 1316–1333 (2009).
42. Chiang, E. I. & Goldreich, P. Spectral energy distributions of T Tauri stars with passive circumstellar disks. *Astrophys. J.* **490**, 368–376 (1997).
43. Okuzumi, S., Ueda, T. & Turner, N. J. A global two-layer radiative transfer model for axisymmetric, shadowed protoplanetary disks. *Publ. Astron. Soc. Jpn.* **74**, 828–850 (2022).
44. Carrasco-González, C. et al. The radial distribution of dust particles in the HL Tau disk from ALMA and VLA observations. *Astrophys. J.* **883**, 71 (2019).
45. Hamaker, J. P. & Bregman, J. D. Understanding radio polarimetry. III. Interpreting the IAU/IEEE definitions of the Stokes parameters. *Astron. Astrophys. Suppl. Ser.* **117**, 161–165 (1996).
46. Kataoka, A., Muto, T., Momose, M., Tsukagoshi, T. & Dullemond, C. P. Grain size constraints on HL Tau with polarization signature. *Astrophys. J.* **820**, 54 (2016).
47. Hildebrand, R. H. et al. A primer on far-infrared polarimetry. *Publ. Astron. Soc. Pac.* **112**, 1215–1235 (2000).
48. Cox, E. G. et al. High-resolution 8 mm and 1 cm polarization of IRAS 4A from the VLA Nascent Disk and Multiplicity (VANDAM) survey. *Astrophys. J. Lett.* **814**, L28 (2015).
49. Cox, E. G. et al. ALMA's polarized view of 10 protostars in the Perseus Molecular Cloud. *Astrophys. J.* **855**, 92 (2018).
50. Kwon, W. et al. Highly ordered and pinched magnetic fields in the class 0 protobinary system L1448 IRS 2. *Astrophys. J.* **879**, 25 (2019).
51. Le Gouellec, V. J. M. et al. A statistical analysis of dust polarization properties in ALMA observations of Class 0 protostellar cores. *Astron. Astrophys.* **644**, A11 (2020).
52. Bacciotti, F. et al. ALMA observations of polarized emission toward the CW Tau and DG Tau protoplanetary disks: constraints on dust grain growth and settling. *Astrophys. J. Lett.* **865**, L12 (2018).
53. Mori, T. et al. An observational study for grain dynamics in the AS 209 disk with submillimeter polarization. *Astrophys. J.* **883**, 16 (2019).
54. Sadavoy, S. I. et al. Dust polarization toward embedded protostars in Ophiuchus with ALMA. III. Survey overview. *Astrophys. J. Suppl. Ser.* **245**, 2 (2019).
55. Harrison, R. E. et al. ALMA CN Zeeman observations of AS 209: limits on magnetic field strength and magnetically driven accretion rate. *Astrophys. J.* **908**, 141 (2021).
56. Dent, W. R. F. et al. Submillimetre dust polarization and opacity in the HD163296 protoplanetary ring system. *Mon. Not. R. Astron. Soc. Lett.* **482**, L29–L33 (2019).
57. Robitaille, T. & Bressert, E. APLpy: Astronomical Plotting Library in Python (Astrophysics Source Code Library, 2012).

Acknowledgements ALMA is a partnership of ESO (representing its member states), NSF (USA) and NINS (Japan), together with NRC (Canada), MOST and ASIAA (Taiwan) and KASI (Republic of Korea), in cooperation with the Republic of Chile. The Joint ALMA Observatory is operated by ESO, AUI/NRAO and NAOJ. The National Radio Astronomy Observatory is a facility of the National Science Foundation operated under a cooperative agreement by Associated Universities. Z.-Y.D.L. acknowledges support from NASA 80NSSC18K1095, the Jefferson Scholars Foundation, the NRAO ALMA Student Observing Support (SOS) SOSPA8-003, the Achievements Rewards for College Scientists (ARCS) Foundation Washington Chapter, the Virginia Space Grant Consortium (VSGC) and the UVA research computing (RIVANNA). Z.-Y.L. is supported in part by NASA 80NSSC20K0533 and NSF AST-2307199. L.W.L. and R.H. acknowledge support from NSF AST-1910364 and NSF AST-2307844. C.C.-G. acknowledges support from UNAM DGAPA-PAPIIT (grant no. IG101321) and from CONACyT Ciencia de Frontera (project ID 86372). R.T. acknowledges financial support from the CNES fellowship.

Author contributions This project was led by I.W.S. Polarization modelling was performed by Z.-Y.D.L. Data reduction was performed by M.F.-L. All authors analysed and discussed the observations and contributed to the paper.

Competing interests The authors declare no competing interests.

Additional information

Correspondence and requests for materials should be addressed to Ian W. Stephens.

Peer review information *Nature* thanks the anonymous reviewers for their contribution to the peer review of this work.

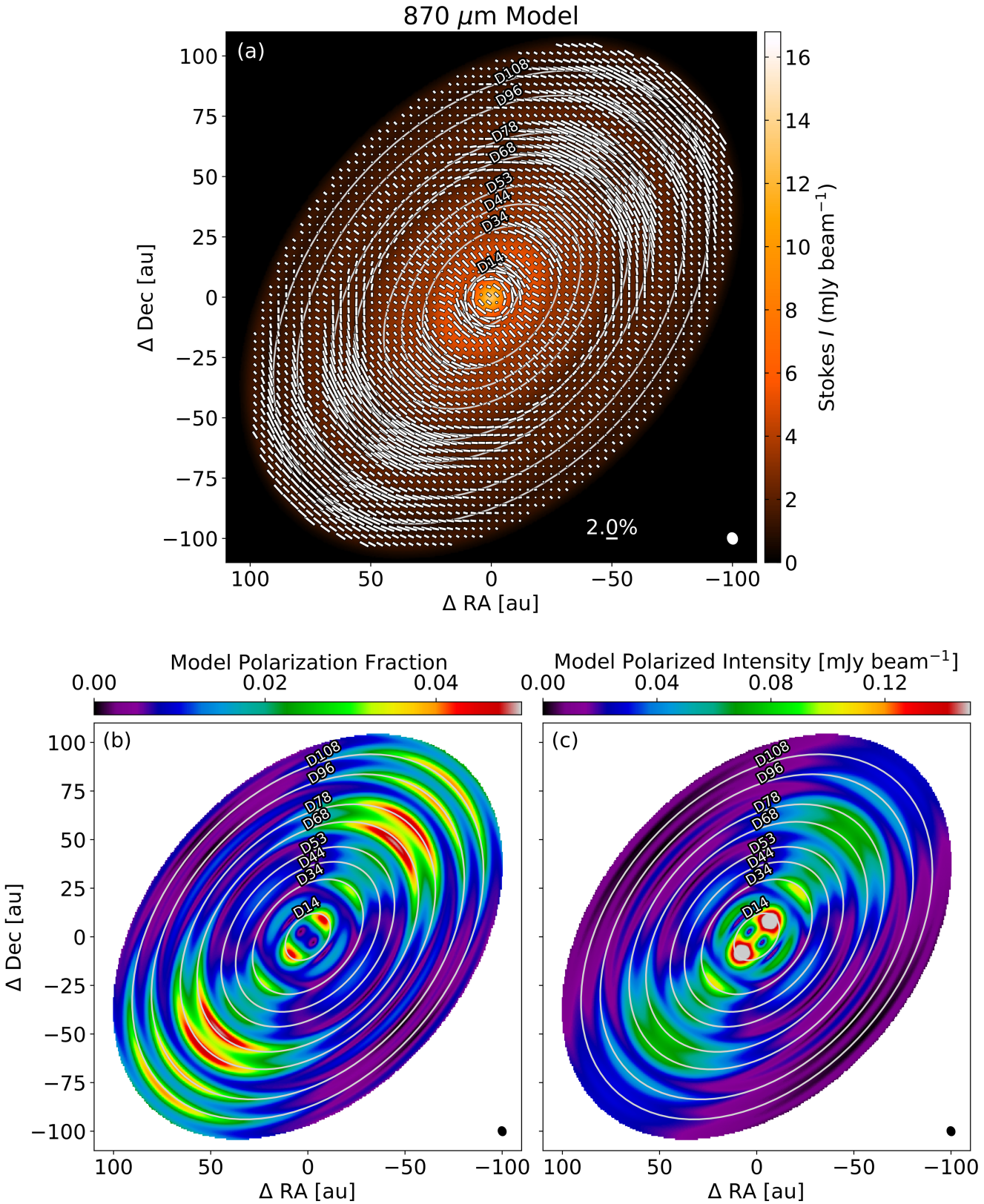

Extended Data Fig. 1 | Polarization images of the model. a, The colormap is the Stokes *I* image in mJy beam^{-1} and the line segments represent the polarization angle. The length of the segments are proportional to the polarization fraction with a 2% scale bar shown in the bottom. **b**, The linear polarization fraction image. **c**, The linear polarized intensity in mJy beam^{-1}. The resolution is shown as a small white or black ellipse in the bottom right of each panel. The concentric ellipses on top of the disk mark the location of the gaps.

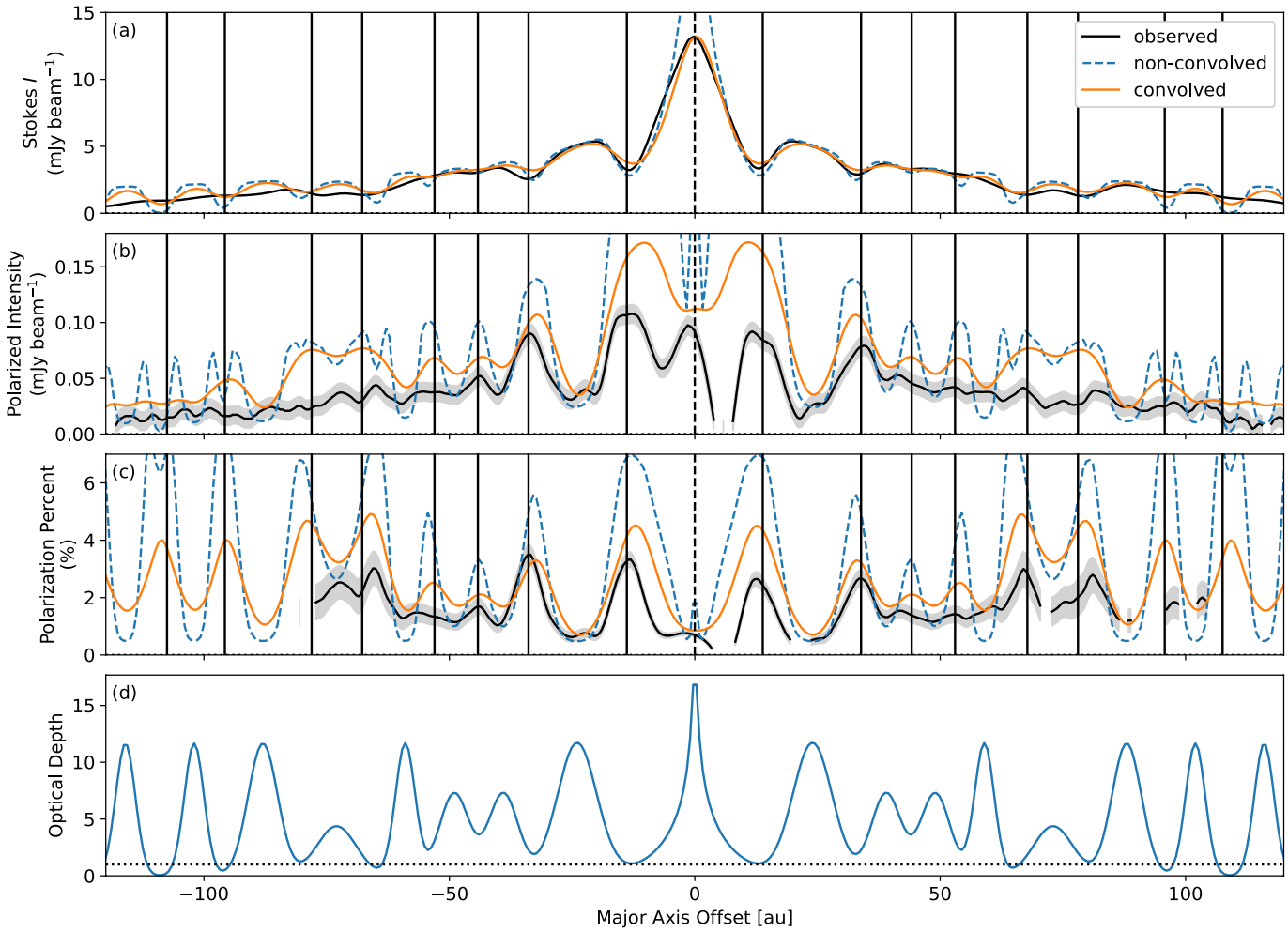

Extended Data Fig. 2 | Comparisons of the profiles along the major axis between the observation and model. The first three panels show the Stokes *I* (panel a), linear polarized intensity (panel b), and the linear polarization fraction (panel c). The observations are plotted in black solid lines with shaded areas showing the standard deviation. The dashed blue lines show the model profiles prior to beam convolution and the orange solid lines show the model profiles after beam convolution. Panel d shows the input optical depth of the model. The horizontal dotted line is where the optical depth is 1. The vertical solid lines mark the locations of the gaps.

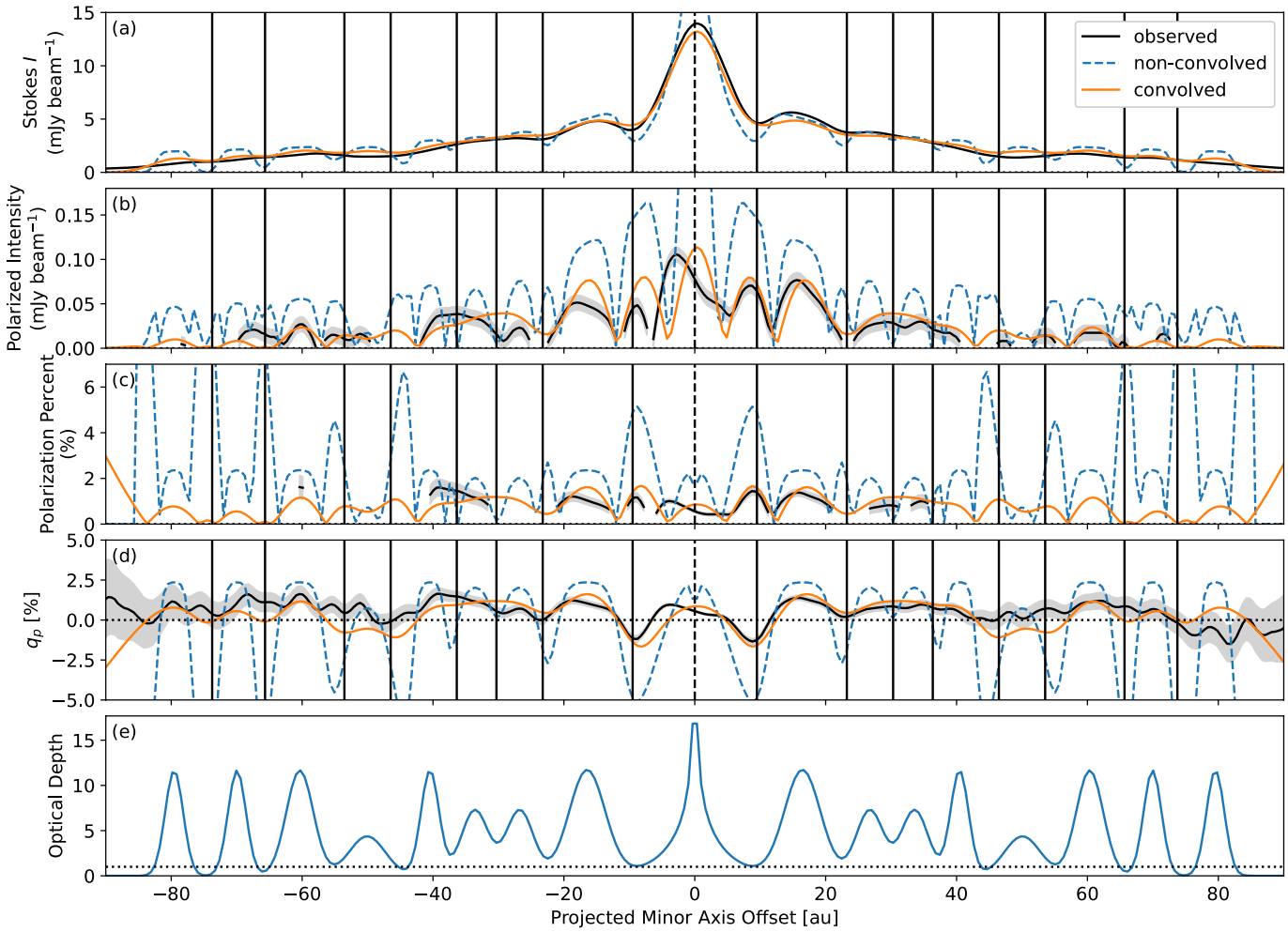

Extended Data Fig. 3 | Profiles along the minor axis. These are plotted in a similar way as Extended Data Fig. 2. The additional panel d shows q_p (see text for the definition). The positive offset is towards the northeast direction.

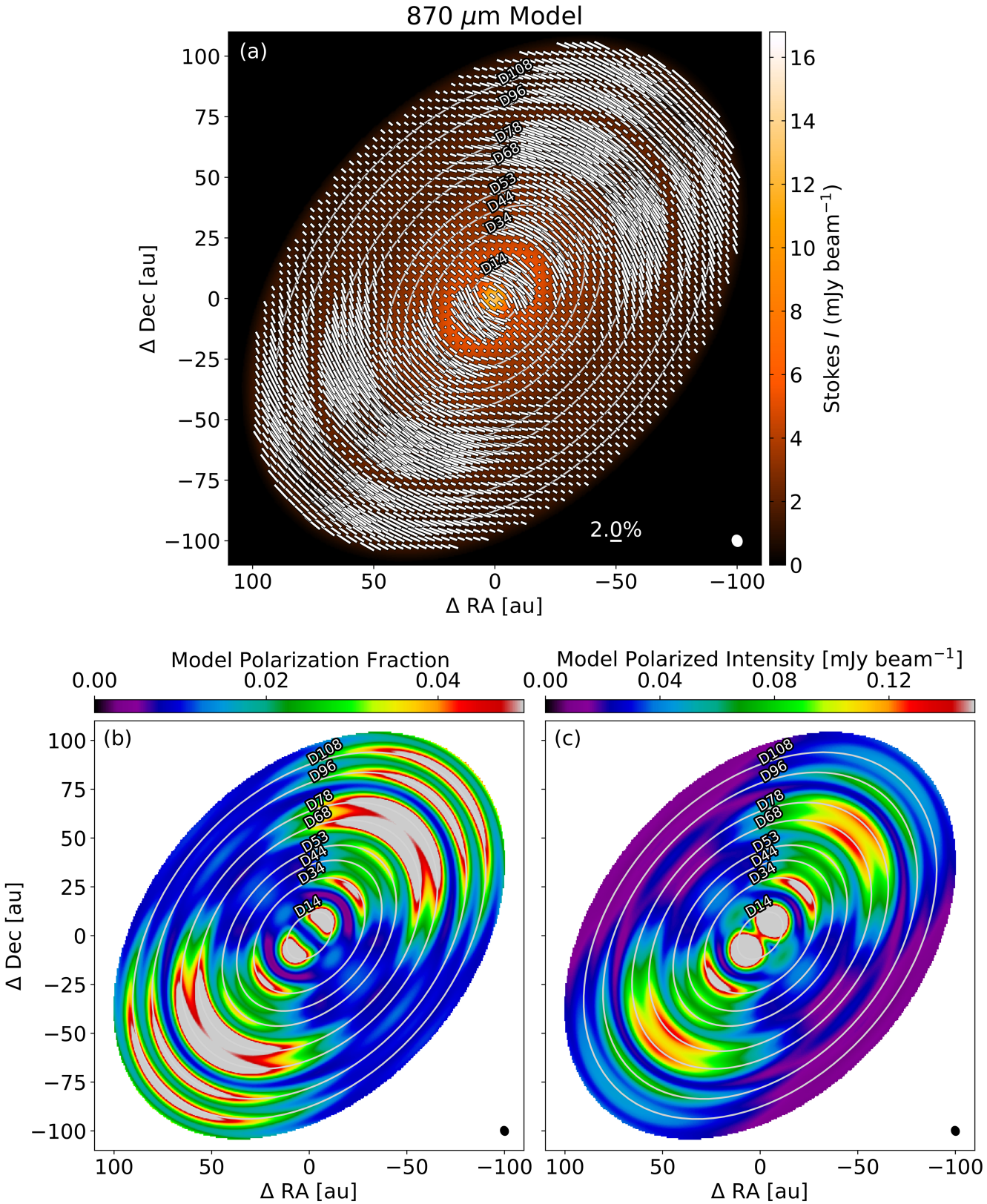

Extended Data Fig. 4 | Model using effectively oblate grains. Figure caption is the same as Extended Data Fig. 1, but now with oblate grains. The color scales in panels b and c have been saturated at many locations so that the morphologies of the low-level polarization fractions and intensities are visible.

Extended Data Table 1 | The parameters used to produce the disk model and polarization image

T_{10} [K]	110							
$a_{\max}$ [μm]	100							
s	0.85							
R_0 [au]	10							
τ_a	2.3							
p	0.5							
C [au]	24	39	49	59	73	88	102	116
τ_c	8	5	5	8	3	8	8	8
W [au]	4	3	3	2	4	3	2	2